communications earth & environment

A Nature Portfolio journal

Article

https://doi.org/10.1038/s43247-026-03954-6

Global drought shows no detectable recent acceleration under climate warming

Check for updates

Jiameng Xu[1,2,9], Xiao Zhang[1,2,9], Kaighin A. McColl[3,4], Alexis Berg[5], Sha Zhou[6,7], Jian Yang[8], Zhaoyu Dong[1,2], Yuanyuan Luo[1,2] & Yuanchao Fan[1,2] ✉

Recent studies suggest that warming is accelerating continental drought, but these conclusions rely on drought indices using Penman-type potential evapotranspiration (PET). While Penman-type PET is widely used and may suit non-water-limited or irrigated surfaces, it can overstate evaporative demand at broader spatial scales by neglecting land-atmosphere coupling constraints; energy-based PET formulations can address this limitation. Applying multiple PET formulations to calculate the Standardized Precipitation Evapotranspiration Index (SPEI) over 1981–2024, we show that Penman-type methods artificially inflate PET contributions to SPEI trends, resulting in drying trends at least six times stronger than energy-based SPEIs across drought severity, frequency, and duration. We find no significant acceleration of drought trends across ~99% of quasi-global land area under either PET type. This finding remains robust across centennial timescales (1901– or 1950–2024). Reported drought acceleration therefore largely reflects unconstrained PET methods and imprecise analytical frameworks, rather than a true ecohydrological response to warming, with important implications for climate risk assessment and adaptation planning.

Drought is a major constraint on freshwater availability, ecosystem functioning, and food security[1–4], and its evolution under global warming remains a central concern in climate impact assessments[5–7]. Numerous studies have reported increasing drought severity and expanding drought-affected areas over recent decades[8–12], drawing on converging evidence from multivariate atmospheric drought indices, which combine precipitation with atmospheric evaporative demand (potential evapotranspiration (PET), calculated from near-surface atmospheric variables) to infer surface drought conditions[5,11,13], together with independent, hydrological evidence such as observation-calibrated soil moisture reconstructions[14], remotely sensed terrestrial water storage[15], and observed streamflow declines[16]. However, substantial quantitative uncertainties remain specifically in the magnitude of drought trends inferred from PET-based drought indices, as such inferences depend critically on how atmospheric evaporative demand is estimated[17–20]. Given that PET-based indices remain among the most widely used tools for characterizing large-scale, long-term drought variability owing to their global data coverage and standardized formulation, these uncertainties arguably affect our ability to anticipate future hydroclimatic impacts and complicate downstream adaptation decision-making.

Beyond the qualitative consensus of drought intensification, whether hydroclimatic extremes are accelerating (i.e., intensifying at an increasing rate) has recently emerged as a pertinent scientific question, motivated by two related lines of evidence: recent reports that global surface warming itself may be accelerating[21], and projections of intensifying hydroclimatic extremes under continued warming[22]. In this context, a recent study explicitly claimed that warming is driving a widespread acceleration of continental drought severity[8]. However, the conclusion[8] relies almost exclusively on trend detection using drought indices derived from Penman-type PET formulations, which lack physical constraints from land–atmosphere feedbacks. This raises a critical question: under the ongoing acceleration of global surface warming, does continental drought

[1]Institute of Environment and Ecology, Tsinghua Shenzhen International Graduate School, Tsinghua University, Shenzhen, China. [2]Key Laboratory of Ecological Carbon Fixation and Sink Enhancement in Ordinary Universities of Guangdong Province, Guangzhou, China. [3]Department of Earth and Planetary Sciences, Harvard University, Cambridge, MA, USA. [4]School of Engineering and Applied Sciences, Harvard University, Cambridge, MA, USA. [5]Department of Geography, Université de Montréal, Montreal, QC, Canada. [6]State Key Laboratory of Earth Surface Processes and Disaster Risk Reduction, Faculty of Geographical Science, Beijing Normal University, Beijing, China. [7]Institute of Land Surface System and Sustainable Development, Faculty of Geographical Science, Beijing Normal University, Beijing, China. [8]Department of Forestry and Natural Resources, University of Kentucky, Lexington, KY, USA. [9]These authors contributed equally: Jiameng Xu, Xiao Zhang. ✉e-mail: yuanchao.fan@sz.tsinghua.edu.cn

severity indeed accelerate as a physical reality, or is it an artifact of analytical frameworks and how atmospheric evaporative demand is estimated?

A key component underlying most drought index-based assessments is the representation of PET, which quantifies atmospheric evaporative demand and constitutes the primary pathway through which rising air temperature and associated vapor pressure deficit (VPD) influence the magnitudes and trends of drought indices under global warming[20,23,24]. However, PET is not directly observable and is therefore estimated using idealized, theoretical formulations that make distinct assumptions about atmospheric demand, surface resistance, land–atmosphere coupling, and related processes[25,26]. As a result, drought and aridity indices based on different PET formulations, including Penman[25], Thornthwaite[27], Penman–Monteith[26], and energy-based approaches[23,28,29], among others, can yield substantially different magnitudes and, in some cases, even opposite trends of drought[18,20,23,30].

The Penman–Monteith (PM) equation[26] and related PET formulations[25,31,32] (hereafter Penman-type PETs) are widely adopted because they provide physically comprehensive estimates of evaporative demand by integrating both radiative energy supply and aerodynamic vapor transport processes. These formulations perform well under their original design context: estimating evaporation from small, well-watered surfaces such as reference crops or evaporation pans, where local evapotranspiration does not substantially alter overlying atmospheric conditions[25,32]. However, when applied to large-scale drought assessment over water-limited regions, Penman-type PETs systematically overestimate continental drying[12,18,23,28–30]. Observational[33] and modeling simulations[23,34] have shown that Penman-type PETs often exceed observed or estimated non-water-stressed evapotranspiration. This bias arises because they estimate evaporation from an assumed wet surface (unlimited moisture supply) while using observed near-surface atmospheric states (Eq. (1)). Under dry land surface conditions, this approach neglects critical land–atmosphere feedbacks: reduced soil moisture suppresses actual evapotranspiration, which in turn decreases local atmospheric humidity and increases air temperature, thereby inflating VPD[29,34–36] (see schematic in Supplementary Fig. 1). Crucially, this unconstrained reliance on atmospheric states exposes Penman-type metrics to the exponential non-linearity of the Clausius-Clapeyron relationship. As temperatures rise, the non-linear acceleration in VPD is directly translated into an artificially accelerating evaporative demand, which in turn, purportedly, drives an acceleration of drought conditions globally[28,34]. By contrast, energy-based PET formulations explicitly constrain evaporative demand by surface energy availability and better capture surface–atmosphere coupling—for example, by formulating PET directly as a function of net radiation or by introducing surface resistance, evaporative fraction, or Bowen-ratio-based terms that depend on surface temperature and humidity gradients (Eqs. (11)–(15)). These approaches better account for soil moisture limitations on land–atmosphere exchanges, thereby yielding physically consistent estimates of evaporative demand and drought indices, particularly under large-scale, water-limited conditions[23,28,29,35].

In real-world land–atmosphere coupling[37,38], surface drying is typically accompanied by rising air temperature and increasing VPD, while evaporative fluxes remain constrained by surface energy and water availability[36]. This simultaneous intensification of atmospheric demand and limitation of surface evaporation highlights a fundamental conflict between aerodynamic and energy constraints[28,29,34]. Differences in how PET formulations represent this coupling have been widely implicated in the "aridity paradox", whereby observed vegetation activity and ecosystem water status appear inconsistent with drying trends inferred from drought indices calculated with Penman-type PETs[18,39–44]. While the physical mechanisms driving Penman-type PET inflation biases are now well-established[23,34,42,45], the extent to which these biases distort the temporal evolution and potential acceleration of historical drought trends remains critically under-quantified.

Despite growing recognition of uncertainties in PET estimation, existing studies have primarily focused on how different PET formulations affect aridity conditions or projected long-term trends in future scenarios[18]. Much less attention has been paid to how Penman-type and energy-based PET formulations influence the temporal evolution of drought in observations, including trends in drought severity, frequency, duration, and impacted area, as well as potential acceleration (i.e., intensifying at an increasing rate). Moreover, detecting such second-order trends is inherently challenging and warrants rigorous statistical scrutiny. For example, the aforementioned conclusion of warming-driven drought acceleration[8] was based on comparing drought trends between two arbitrarily selected time periods (1981–2017 vs. 2018–2022), a method highly sensitive to inter-annual variability and changepoint selection[46]. To reliably test the acceleration hypothesis and separate it from internal climate variability, it is imperative to employ robust statistical testing over extended observational records. These methodological gaps motivate the present study.

Here, we analyze quasi-global drought evolution from 1981 to 2024 based on the 6-month Standardized Precipitation Evapotranspiration Index (SPEI) calculated using six widely applied PET formulations, grouped into Penman-type and energy-based categories. We systematically quantify trends in drought severity, affected area, drought frequency, and duration. Crucially, we examine the acceleration or deceleration of drought trends using the modified Mann–Kendall (MMK) test to rigorously account for temporal autocorrelation, with the statistical power of this detection framework further validated through synthetic Monte Carlo simulations. To ensure robustness against multidecadal climate variability, we extend our analysis using historical records dating back to 1950 and 1901. Furthermore, we conduct an attribution analysis to isolate the relative contributions of precipitation and varying PET methodologies to the overall drought trends. In this way, our study provides a more physically consistent assessment of drought trends and acceleration under recent warming. Our results reveal that there is no detectable recent acceleration in global drought. Instead, we demonstrate that the magnitude of inferred drought intensification is predominantly an artifact of the sensitivity of the chosen PET formulations, with important implications for assessing future drought risk and informing climate adaptation actions.

Results

Penman-type SPEIs overstate global drought trends

We calculated 6-month SPEIs using two combinations of underlying precipitation (CHIRPS and MSWEP) and meteorological datasets (MSWX100 and ERA5-Land) from 1981 to 2024. PET was estimated using three Penman-type formulations, including Penman[25] (PE), Penman equation for open water surfaces (PE-OW)[31], and Penman–Monteith for reference crop[32] (PM-RC), and three energy-based formulations, including Milly and Dunne[23] (MD), Yang and Roderick[29] (YR), and Zhou and Yu[28] (ZY) for each of the two meteorological datasets, yielding 11 unique PETs and corresponding SPEIs (see "Methods" subsection "Datasets"). Hereafter, the SPEIs calculated with Penman-type PETs (PE, PE-OW, PM-RC) are referred to as Penman-type SPEIs, and those calculated with energy-based PETs (MD, YR, ZY) are referred to as energy-based SPEIs. The resulting quasi-global (50°S–50°N) area-weighted mean 6-month SPEI trend of Penman-type methods is $-0.0084\,\mathrm{yr}^{-1}$ (95% Confidence Interval (CI): -0.0092 to -0.0076, $P < 0.0001$), indicating a statistically significant intensification of drought (Fig. 1a). Penman-type PET formulations incorporate both radiative and aerodynamic terms but neglect land-atmosphere coupling constraints, thereby overestimating atmospheric evaporative demand under warming[29,34–36]. In contrast, the quasi-global SPEI trend calculated with energy-based PET formulations[23,28,29] weakens to $-0.0014\,\mathrm{yr}^{-1}$ (95% CI: -0.0021 to -0.0006, $P = 0.0003$), ~83.33% smaller than trends derived from Penman-type methods (i.e., a 6-fold difference) (Fig. 1a). Similarly, the trends in the quasi-global percentage of land area affected by drought (SPEI < -1) show notable differences between the two types of methods—Penman-type SPEIs show an average trend of $0.2406\%\,\mathrm{yr}^{-1}$ (95% CI: 0.2138–0.2678, $P < 0.0001$), about 7.76 times larger than that of the energy-based SPEIs ($0.031\%\,\mathrm{yr}^{-1}$, 95% CI: 0.0071–0.0547, $P = 0.0113$) (Fig. 1b).

Beyond the contrast in ensemble-mean trends, Fig. 1c further reveals a clear separation in both the magnitude and uncertainty of drought trends

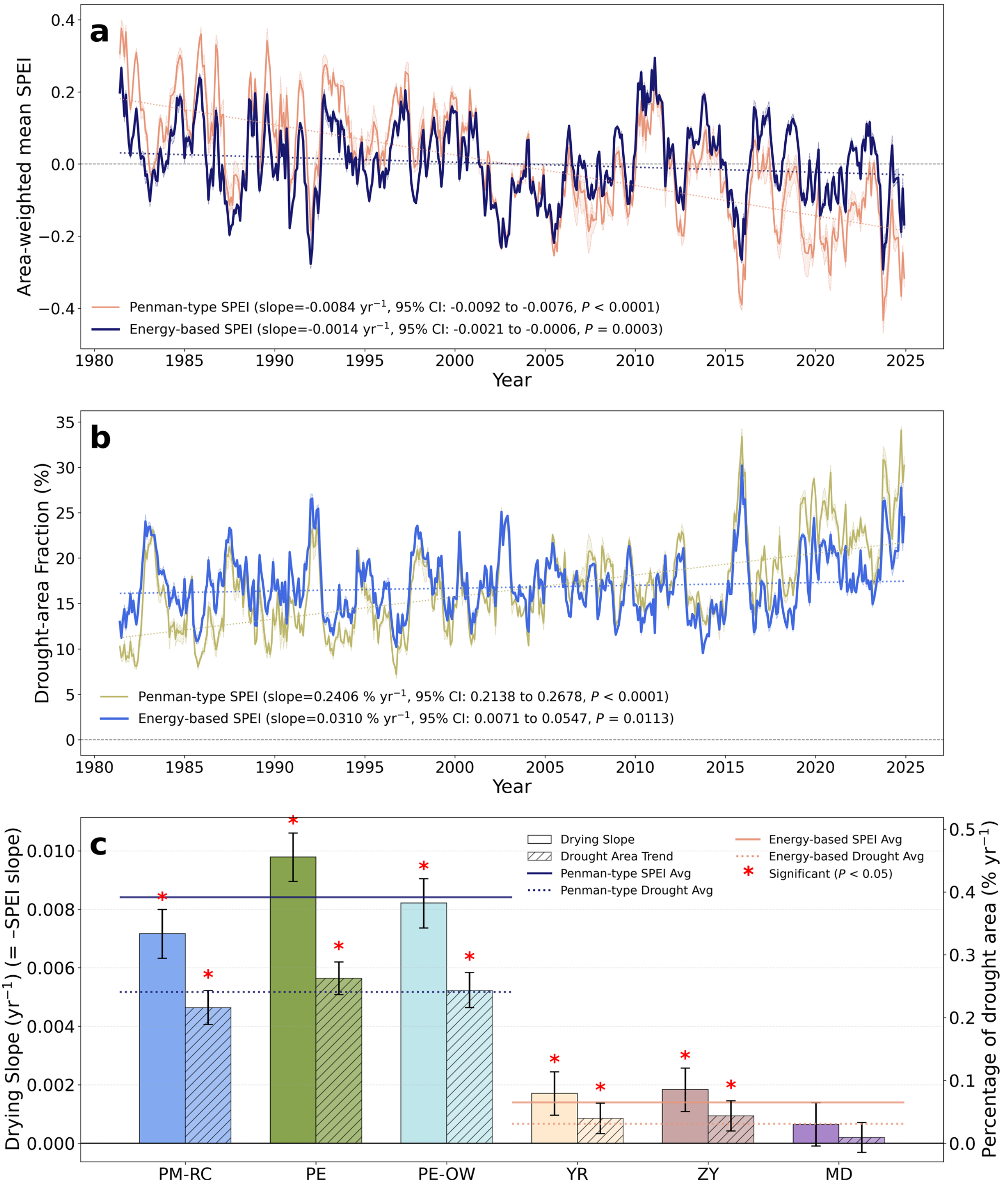

between the two types of PET formulations. All three Penman-type methods consistently produce strong and statistically significant drying trends in both SPEI and drought area, indicating a strong response to warming-driven atmospheric demand. In contrast, energy-based SPEIs exhibit substantially weaker trends, with the MD method showing insignificant trends in both SPEI and drought area. This divergence is amplified in drought area trends, where Penman-type methods yield drought area increases exceeding energy-based estimates by ~8-fold (Fig. 1b and c). The clear clustering of methods within each PET category, together with the separation between two categories, suggests that the uncertainty in global drought estimation is primarily controlled by the structural difference in the treatment of evaporative demand in two types of PET formulations rather than by individual PET implementations.

Despite the overall drying trends inferred from both PET categories over 1981–2024, the quasi-global SPEI exhibits a pronounced non-monotonic temporal evolution. The time series features multiple short-term fluctuations (e.g., during 2015–2016), with one of the more notable declines occurring during the 2000–2003 period (Fig. 1a). This timing is

Fig. 1 | Monthly SPEI and SPEI trends derived from Penman-type and energy-based PET methods from 1981 to 2024. The quasi-global (50°S–50°N) average SPEI (**a**) and global percentage of area in droughts (**b**). The thick solid lines represent the group ensemble means, the dotted lines represent their corresponding overall trends, and the shaded envelopes, which bound the thin dashed lines showing the trajectories of individual PET calculation methods, denote the full range (minimum to maximum envelope) within each group (Penman-type and energy-based), reflecting uncertainty arising from methodological choices. For panels **a** and **b**, statistical trend analyses and slope calculations are based on monthly data points ($n = 523$ independent months from June 1981 to December 2024). **c** Bar charts comparing drying slopes (represented as inverted SPEI trends, −SPEI trend) and drought-area trends across individual PET methods in the two categories (Penman-type and energy-based). Error bars represent the 95% confidence intervals of the trend estimates derived from two-sided Theil–Sen slope analysis. The asterisks (*) indicate trends that are statistically significant at the $P < 0.05$ level based on the two-sided Mann–Kendall test. Exact P values for all trends shown in panel **c** are as follows (SPEI trend/drought-area trend): PM-RC ($P < 10^{-15}$/$P < 10^{-15}$), PE ($P < 10^{-15}$/$P < 10^{-15}$), PE-OW ($P < 10^{-15}$/$P < 10^{-15}$), YR ($P = 1.14 \times 10^{-5}$/$P = 0.0012$), ZY ($P = 2.2 \times 10^{-6}$/$P = 0.0004$), MD ($P = 0.088$/$P = 0.4488$), Penman-type ensemble ($P < 10^{-15}$/$P < 10^{-15}$), energy-based ensemble ($P = 0.0003$/$P = 0.0113$). The exact trend values and P values are also provided in Supplementary Table 1. Trend estimates for each PET formulation are derived from $n = 523$ independent monthly SPEI/drought-area values (June 1981–December 2024), based on ensemble means across $n = 2$ independent dataset combinations (MSWEP_MSWX100 and CHIRPS_ERA5), except for the Penman method (PE), which is based on $n = 1$ dataset (MSWEP_MSWX100). This exception is because the Penman equation involves calculations of aerodynamic conductance, where self-computation may introduce significant errors. We therefore directly utilize PET outputs from GLEAM[68], which primarily employs MSWX100 as its meteorological data source, with missing variables supplemented by ERA5-Land. The results cover quasi-global land areas (50°S–50°N) as CHIRPS is available up to 50°N and excluding regions with average annual rainfall below 180 mm. Each SPEI dataset is masked using the precipitation mask of its respective precipitation product. For panels **a** and **b**, ensemble means are first calculated across dataset combinations for each individual PET formulation, and then averaged across PET formulations within each PET group. For panel **c**, trends are shown for individual PET formulations, with ensemble means calculated across dataset combinations for each method.

consistent with previous reports of a large-scale transfer of terrestrial water storage to the oceans[47]. The breakpoint at 2003 is used here as an illustrative example rather than a statistically unique change point. Following this period, Penman-type SPEI trends show a slight weakening after 2003 (Supplementary Fig. 2), while energy-based SPEIs shift from a significant drying trend (−0.003 yr^{-1}, 95% CI: −0.005 to −0.001, $P = 0.012$) to a weak and statistically insignificant wetting trend (0.001 yr^{-1}, 95% CI: −0.001 to 0.003, $P = 0.545$; Supplementary Fig. 2). Despite possible redistribution of land water during 2000–2003, continental drought conditions did not subsequently intensify and, as reflected by the energy-based SPEIs (Supplementary Fig. 2), even exhibited partial recovery. These temporal contrasts motivate an explicit assessment of long-term changes in drought trends by the following acceleration analysis (next section).

Spatially, 44.39% of the quasi-global land area (50°S to 50°N, excluding regions with average annual precipitation below 180 mm) exhibits significantly drying trends according to Penman-type SPEIs (Supplementary Fig. 3a), but this proportion drops to 26.79% when using energy-based SPEIs (Supplementary Fig. 3b). This suggests that a large proportion (46.49%) of previously reported Penman-based drying signals are methodological artifacts, which disappear under the energy-based framework after imposing a physical constraint on evaporative demand. The remaining 53.51% of Penman-inferred drying areas spatially overlap with the energy-constrained drying areas, demonstrating that localized drought intensification remains a verifiable regional reality across different drought metrics. As expected, these persistent drying hotspots are predominantly located in precipitation-limited regions, including parts of South America, the Mediterranean basin, localized areas in Eurasia, and western Australia. On the other hand, the percentage of land area exhibiting wetting trends increases from 14.16% by Penman-type SPEIs to 23.15% by energy-based SPEIs. As a result, the net percentage of land area with drying trends decreases from 30.23% by Penman-type SPEIs to only 3.64% by energy-based SPEIs. Key regions contributing to this difference, including the southern Sahel, southern Africa, northern China, and central-northern Australia, exhibit a transition from significant drying (or non-significant changes) under Penman-type methods to pronounced wetting trends under energy-based SPEIs (Supplementary Fig. 3a and b). This divergence between Penman-type and energy-based SPEI trends also shows a clear dependence on hydroclimatic conditions, with drier regions exhibiting larger differences and wetter regions showing minimal divergence (Supplementary Figs. 4 and 5). This pattern reflects the stronger water limitation in arid areas, where Penman-type PETs overestimate evaporative demand, while energy constraints dominate in humid regions, reducing methodological differences. Overall, such a large divergence in the temporal trend and spatial pattern (Supplementary Fig. 3c) implies that the global extent of drying trends has been overestimated based on traditional Penman-type PET formulations.

To further understand the underlying drivers of these diverging drought trends, we conducted a trend attribution analysis to decompose the relative contributions of precipitation and PET to the overall SPEI trends (Supplementary Figs. 6 and 7). Under Penman-type formulations, PET accounts for nearly half (47.5%) of the global drought trend contribution, competing closely with precipitation (52.5%). However, under energy-based SPEIs, the contribution of PET is nearly halved to 25%, restoring precipitation to its fundamental role as the overwhelmingly dominant driver (75%) of long-term hydroclimatic variations. Spatially, the PET contributions in Penman-type SPEIs are particularly pronounced across arid and semi-arid regions (Supplementary Fig. 7b), whereas energy-based metrics reveal a much more constrained PET influence globally (Supplementary Fig. 7d). This attribution confirms that the severe drying trends inferred from Penman-type metrics are largely artifacts of inflated PET sensitivity.

To provide a more comprehensive assessment, we incorporated two recently developed physical models[36,48] that impose strict physical constraints on evaporative processes. Unlike uncoupled Penman-type formulations, the Kim et al. [36] framework provides an explicitly coupled PET estimate by jointly solving the surface energy balance and boundary-layer humidity feedbacks, which inherently prevents the artificial inflation of evaporative demand. The SPEI derived from this coupled framework yields a remarkably weak and statistically insignificant quasi-global trend of −0.0004 yr^{-1}, accompanied by a non-significant reduction in the drought-affected area (−0.0019% yr^{-1}) (Supplementary Fig. 8). Furthermore, we analyzed the long-term trend in soil saturation derived from the Gallagher and McColl[48] model, which represents the percentage of soil pore space filled with water. By linking atmospheric aridity to soil saturation solely through surface energy partitioning and precipitation, this model effectively captures realistic physical moisture constraints while avoiding aerodynamic VPD artifacts entirely. The inferred trend in soil saturation shows a negligible and non-significant long-term change (−0.00002 yr^{-1}) (Supplementary Fig. 9). Ultimately, the alignment of these advanced coupled frameworks with our energy-based SPEI estimates confirms that properly constraining surface energy and moisture effectively mitigates the exaggerated drought intensification produced by uncoupled Penman-type methods.

Penman-type SPEIs overstate global drought acceleration

We quantified drought acceleration as the long-term trend of decadal SPEI trends. Specifically, we first computed 10-year moving-window trends in SPEI (yr^{-1}) and drought-area percentage (% yr^{-1}), and then estimated the linear trend across these decadal trends (unit for SPEI acceleration: yr^{-2} and for drought-area-percentage acceleration: % yr^{-2}). To address the reduction of effective degrees of freedom caused by temporal autocorrelation in overlapping moving windows, our trend detection employed the MMK test (see the “Methods” for details). This approach explicitly targets long-term

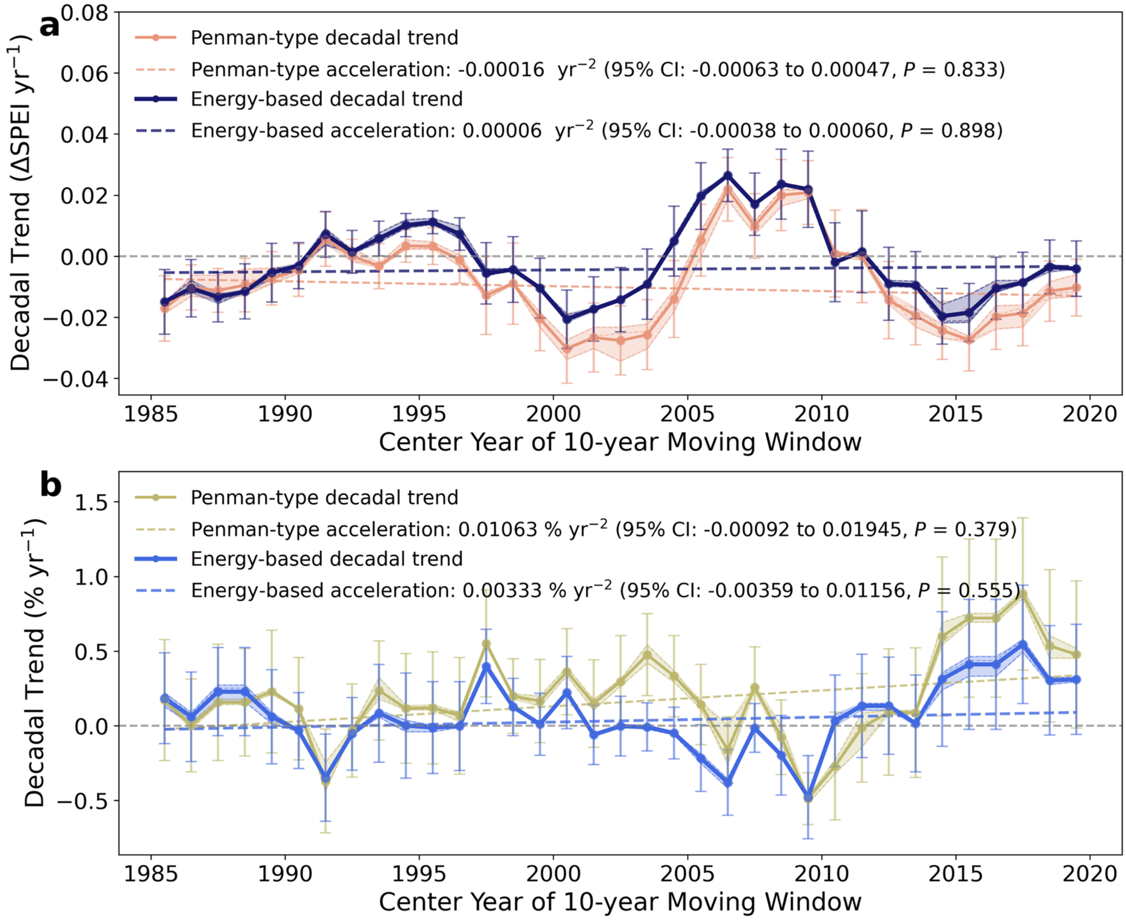

Fig. 2 | Temporal changes in decadal trends (acceleration/deceleration) of SPEI and quasi-global drought-area fraction from 10-year moving windows (1981–2024) using Penman-type SPEIs and energy-based SPEIs. a SPEI and **b** quasi-global drought-area fraction. The thick solid lines represent class-mean decadal trends, and the thin, semi-transparent dashed lines show the decadal-trend trajectories of individual PET calculation methods within each class. The shaded envelopes bound these individual-method trajectories, denoting the full range (minimum–maximum) of decadal trends across methods within each class, and reflecting the structural uncertainty associated with PET formulation choices. Error bars represent ±1 standard error (statistical uncertainty) of the 10-year window's trend estimate. Time series for each PET method were first averaged across the independent datasets (except PE, which relies solely on a single dataset). Decadal trends were then estimated for each individual method using 10-year moving windows. Within each PET class (Penman-type and energy-based), these resulting time series of decadal slopes were averaged across methods to produce the class-mean trend. Acceleration is defined as the overall linear trend of these class-mean decadal slope time series. The displayed acceleration estimates include the 95% confidence intervals (CI) derived from two-sided Theil–Sen slope analysis, based on $n = 35$ 10-year moving windows (1981–2024).

changes in the rate of drought intensification while minimizing the influence of short-term variability (e.g., El Niño events)[49].

As shown in Fig. 2, the inferred acceleration of drought trends varies across PET types when diagnosed from the temporal evolution of moving decadal SPEI and drought-area trends. Although both Penman-type and energy-based SPEIs display significant negative long-term (first-order) trends indicating drought intensification over 1981–2024 (Fig. 1a), the temporal evolution of decadal trends (second-order behavior) reveals no statistically significant acceleration in either type of formulation (Fig. 2a). Specifically, Penman-type SPEI decadal trends show a non-significant negative second-order trend ($-0.00016\ \mathrm{yr}^{-2}$, 95% CI: -0.00063 to 0.00047, $P = 0.833$), whereas energy-based SPEI decadal trends show a non-significant positive second-order trend ($0.00006\ \mathrm{yr}^{-2}$, 95% CI: -0.00038 to 0.0006, $P = 0.898$). Ultimately, neither implies robust acceleration or deceleration in the rate of drought intensification. In addition to the ensemble-mean statistics, none of the individual SPEI datasets show statistically significant second-order trends (Supplementary Fig. 10). Similarly, the inferred acceleration in drought-area trend also shows no statistical significance under either PET type (Fig. 2b). Penman-type SPEIs indicate a non-significant positive acceleration ($0.01063\%\ \mathrm{yr}^{-2}$, 95% CI: -0.00092 to 0.01945, $P = 0.379$), whereas energy-based SPEIs yield a smaller, non-significant acceleration ($0.00333\%\ \mathrm{yr}^{-2}$, 95% CI: -0.00359 to 0.01156, $P = 0.555$) in drought-area trends. Second-order signals thus differ quantitatively between PET types, reflecting SPEI's sensitivity to the choice of PET formulations. Penman-type PET consistently yields lower (more negative) decadal trends than energy-based PET, a pattern also evident in Fig. 2. A two-tailed paired Wilcoxon signed-rank test on the 35 matched 10-year windows confirms this difference is statistically significant for both SPEI and drought-affected area ($P < 0.0001$), despite partial overlap in their overall value ranges (overlap coefficient = 0.802 and 0.788, respectively; two-sample Kolmogorov–Smirnov test, $P = 0.324$ and 0.032; Supplementary Text S1 and Supplementary Fig. 11). More importantly, we find no robust statistical evidence for acceleration in either drought intensity or drought-affected area, regardless of PET formulation.

The absence of global drought acceleration remains a robust historical feature across centennial-scale records. Evaluations over the extended 1950–2024 (ERA5-Land) and 1901–2024 (CRU TS v4.09) periods consistently show no statistically significant acceleration ($P > 0.05$; Supplementary Figs. 12–15). Specifically, SPEI acceleration rates remain negligible across both the 75-year ERA5-Land (-0.00049 and $-0.00043\ \mathrm{yr}^{-2}$ for

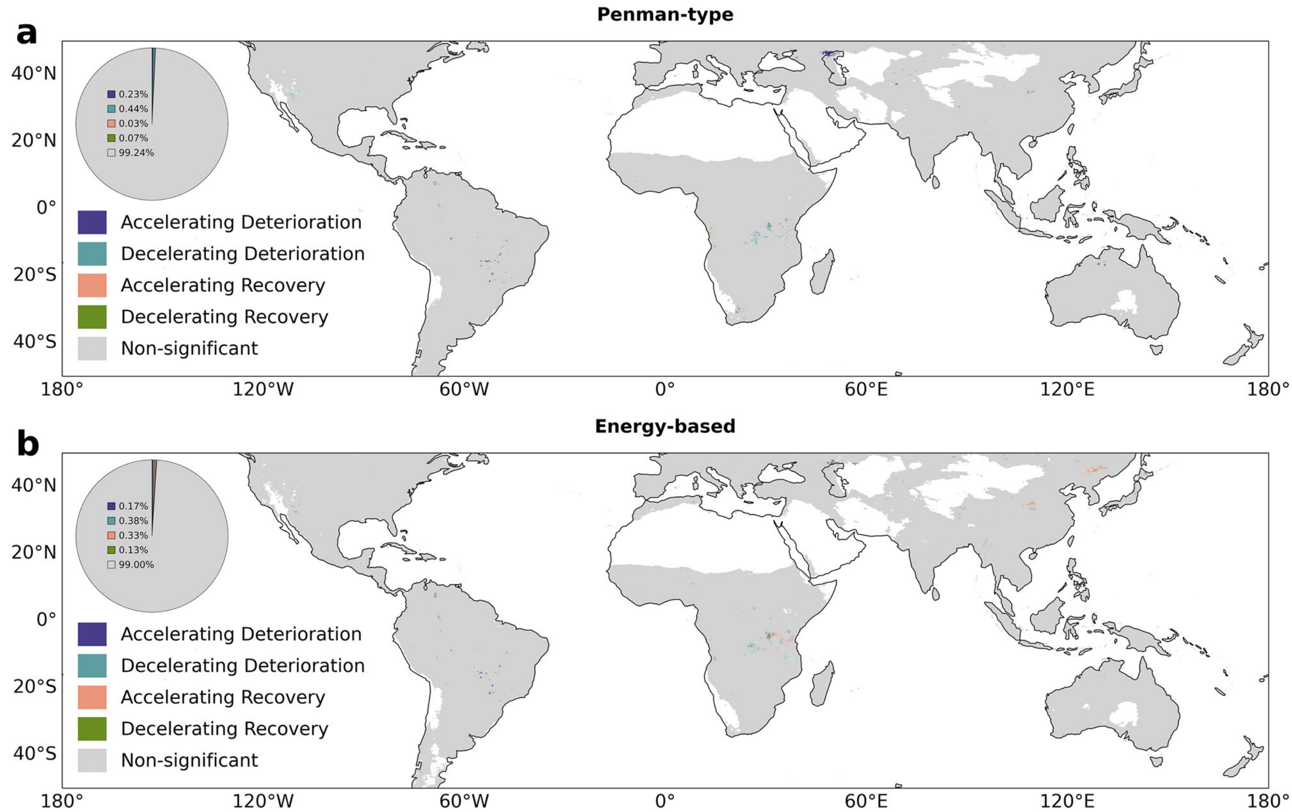

Fig. 3 | Spatial patterns of drought acceleration and deceleration based on Penman-type and energy-based SPEIs during 1981–2024. a Penman-type SPEI and **b** energy-based SPEI. Drought acceleration or deceleration is quantified as the linear trend of decadal SPEI trends estimated using sliding 10-year windows ($n = 35$ overlapping decadal windows), averaged across datasets and PET methods within each formulation class. Signals are interpreted jointly with the sign of the long-term SPEI trend (1981–2024), reflecting changes in the rate of drought intensification or recovery. Drought acceleration/deceleration is classified into four categories by jointly considering the sign of the long-term SPEI trend (first-order trend) and the trend of decadal SPEI trends (second-order acceleration): (1) accelerating deterioration—drought intensifies at an increasing rate (first-order < 0, second-order < 0); (2) decelerating deterioration—drought intensifies, but the rate of intensification is slowing (first-order < 0, second-order > 0); (3) accelerating recovery—drought alleviates at an increasing rate (first-order > 0, second-order > 0); and (4) decelerating recovery—drought alleviates, but the rate of recovery is slowing (first-order > 0, second-order < 0). See the "Methods" section and Supplementary Table 2 for details. Only grid cells where both the first-order SPEI trend and the corresponding acceleration are statistically significant (two-sided modified Mann–Kendall test, $P < 0.05$) are shown, ensuring that the mapped signals represent robust second-order changes. Color intensity denotes the magnitude of acceleration, with darker shades indicating stronger acceleration. Corresponding maps, including all grid cells regardless of significance, are shown in Supplementary Fig. 17.

Penman-type and energy-based methods, respectively) and the 124-year CRU records (−0.00005 yr^{-2}), with corresponding drought area accelerations also remaining statistically non-significant. While the first-order drought trends over these extended periods are weaker than those in the satellite era, Penman-type methods still systematically inflate drought area expansion by more than double compared to energy-based approaches (e.g., 0.0593% vs. 0.0281% yr^{-1} during 1950–2024). These findings demonstrate that the lack of widespread drought acceleration—and the persistent inflation by aerodynamics-dominated metrics—are not artifacts of the 1981–2024 study period, but reflect a consistent physical reality across multiple independent data sources and temporal scales.

This divergence between two types of PETs and corresponding SPEIs is further reinforced by the spatial patterns of drought acceleration or deceleration (Fig. 3, Supplementary Figs. 16 and 17). Here, spatial signals are first characterized by the first-order SPEI trend over 1981–2024 (Supplementary Fig. 3), and further evaluated in terms of acceleration based on the temporal evolution of moving decadal trends. This joint consideration of first- and second-order trends results in four categories of drought dynamics: accelerating deterioration, decelerating deterioration, accelerating recovery, and decelerating recovery (see details in the "Methods" section and Supplementary Table 2). Under Penman-type SPEIs, the majority of the quasi-global land area (99.24%) exhibits no statistically significant acceleration or deceleration signal. Among regions with significant acceleration, some spatially contiguous areas, including central South America, southern Africa, and parts of eastern Europe, exhibit accelerating drought deterioration (Fig. 3a). These regions of drought acceleration account for only 0.23% of all quasi-global land area, while areas characterized by decelerating deterioration occupy nearly twice the proportion (0.44%). Regions associated with accelerating or decelerating drought recoveries remain comparatively limited under Penman-type methods.

Energy-based SPEIs yield a markedly different spatial picture (Fig. 3b). Accelerating drought deterioration is even rarer, accounting for only about 0.17% of quasi-global land area, with pronounced reductions across South America and central Eurasia and near-complete disappearance over southern Africa relative to Penman-type SPEIs. Instead, a larger fraction of regions exhibits either decelerating drought deterioration (0.38%) or accelerating drought recoveries (0.33%). Notably, energy-based SPEIs reveal newly emergent accelerating recovery signals over northern and northeastern China that are largely absent under Penman-type formulations. Under both SPEI types, decelerating drought deterioration dominates over accelerating drought deterioration, resulting in a net reduction of drought deterioration (−0.21% of quasi-global land area) under both Penman-type and energy-based methods (Fig. 3). Energy-based SPEIs capture a larger net increase in drought recoveries (0.2% of quasi-global land area) compared to Penman-type methods. This spatial contraction of drought deterioration or expansion of drought recoveries suggests that previously reported widespread drought acceleration[8] is not a robust feature of long-term

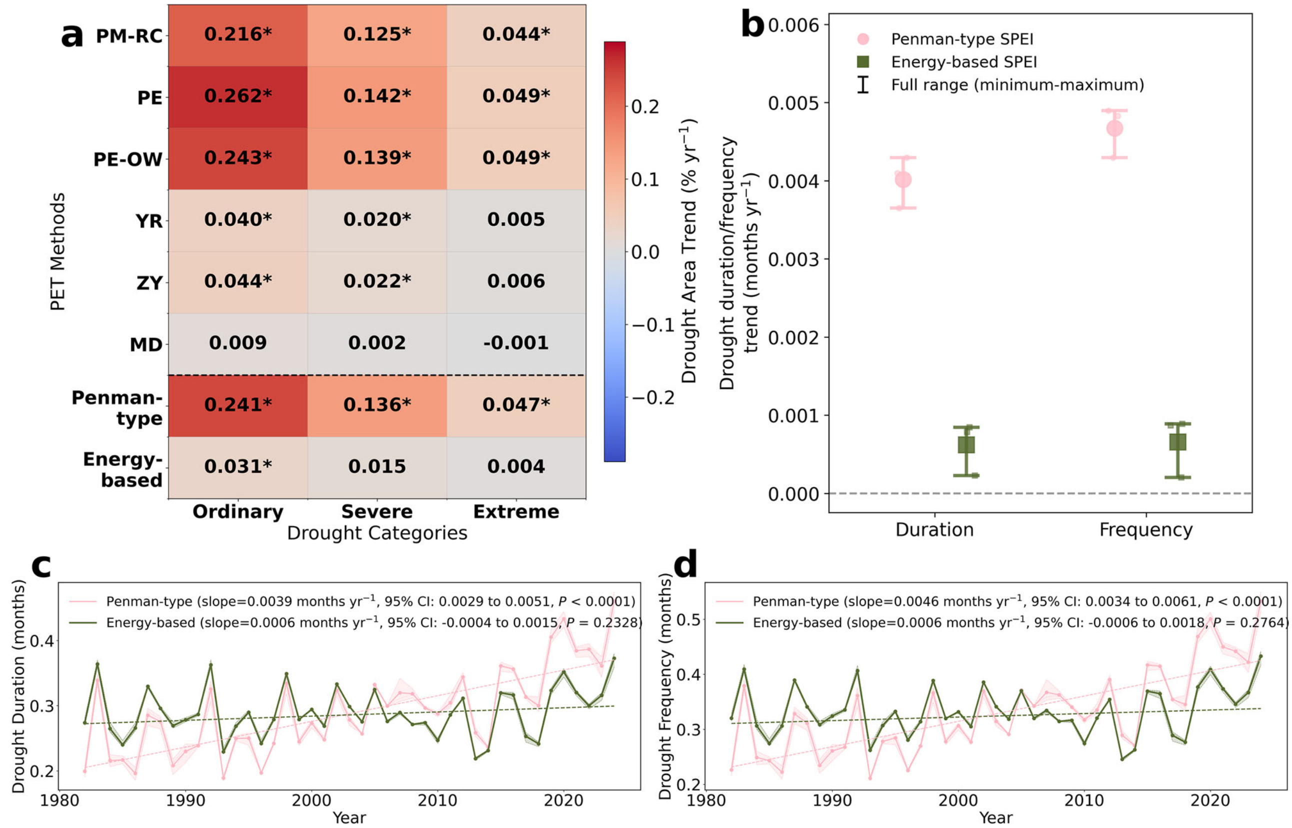

Fig. 4 | PET-dependent contrasts in the monthly trends of drought-area fraction, drought duration, and drought frequency from 1981 to 2024. a Trends in drought-area fraction (% yr^{-1}) for ordinary (SPEI < −1), severe (SPEI < −1.4), and extreme (SPEI < −1.8) droughts based on three Penman-type (PM-RC, PE, PE-OW) and three energy-based (YR, ZY, MD) PET formulations, as well as their ensemble mean. Trend calculations and significance testing are based on monthly records (n = 523 independent months). Asterisks (*) denote statistically significant trends (P < 0.05; two-sided Mann–Kendall test). **b** Comparison of linear trends in global drought duration (defined as the annual maximum length of consecutive months with SPEI < −1; see the "Methods" section) and frequency (defined as the annual number of months with SPEI < −1; see the "Methods" section) (n = 43 years) between Penman-type and energy-based methods. Pink dots and green squares represent ensemble mean trends for Penman-type (dots) and energy-based (squares) SPEI ensembles, respectively. Range bars show the full range (minimum–maximum) of trends of individual PET methods within each ensemble, reflecting the structural uncertainty in SPEI associated with PET formulation choices. Small symbols dispersed around ensemble means indicate trend values of individual PET methods. **c** Global mean drought duration time series derived from Penman-type and energy-based PET formulations (n = 43 years). The thick solid lines represent the group ensemble means, the dotted lines represent their corresponding overall trends, and the shaded envelopes, which bound the thin dashed lines showing the trajectories of individual PET calculation methods, denote the full range (minimum to maximum) of the individual PET methods within each group. **d** same as **c**, but for drought frequency (n = 43 years).

hydroclimatic change, but mainly reflects artifacts of arbitrary changepoint selection and improper assumptions in PET formulations that ignore land–atmosphere coupling constraints on evaporative demand (more in the "Introduction" and "Discussion" sections). Crucially, under both frameworks, an overwhelming majority of quasi-global land areas (≥99%) show no statistically significant acceleration or deceleration signal, reinforcing the lack of a widespread global trend.

Penman-type SPEIs overstate drought characteristics across a wide range of conditions

The PET-dependent divergence systematically extends across ordinary (SPEI < −1), severe (SPEI < −1.4), and extreme (SPEI < −1.8) drought severity classes (Fig. 4). Penman-type SPEIs consistently yield substantially stronger increasing trends in drought area than energy-based SPEIs, regardless of drought intensity. For severe droughts, Penman-type SPEIs yield increasing drought-area trends ranging from 0.125 to 0.142% yr^{-1} across individual formulations, with an ensemble mean of 0.136% yr^{-1}, whereas energy-based SPEIs produce substantially weaker trends (≤0.022% yr^{-1}), many of which are not statistically significant (Fig. 4a). This contrast persists for extreme droughts, where Penman-type SPEIs indicate positive and significant expansion rates (0.044–0.049% yr^{-1}; ensemble mean: 0.047% yr^{-1}) while energy-based SPEIs suggest near-zero changes (−0.001 to 0.006% yr^{-1}), with no statistically significant trend of the ensemble mean (0.004% yr^{-1}, P > 0.05).

The PET methodological contrast is still evident when alternative drought characteristics are considered, including drought duration (defined as the annual maximum length of consecutive drought months) and drought frequency (defined as the annual number of months with SPEI < −1) (Fig. 4b–d and Supplementary Figs. 18 and 19). Global mean drought duration derived from Penman-type SPEIs exhibits a significant increasing trend in the study period (0.0039 months yr^{-1}, P < 0.0001), whereas the corresponding trend based on energy-based SPEIs is much weaker and statistically insignificant (0.0006 months yr^{-1}, P = 0.233; Fig. 4c). A similar pattern emerges for drought frequency (Fig. 4d). Penman-type SPEIs suggest a pronounced increase in global drought frequency (0.0046 months yr^{-1}, P < 0.0001), while energy-based SPEIs again yield a substantially smaller, non-significant trend (0.0006 months yr^{-1}, P = 0.276). Crucially, these relatively weak drought trends and lack of significant acceleration identified by energy-based SPEIs are more consistent with independent ecosystem responses. A detailed ecohydrological analysis—demonstrating widespread, resilient increases in net primary productivity (NPP) and water-use efficiency (WUE) that contradict the exaggerated drought stress inferred by Penman-type methods—is provided in Supplementary Text S2 (and Supplementary Figs. 20 and 21).

Discussion

Our results show that quasi-global SPEI trends are highly sensitive to PET formulation, with energy-based PETs and corresponding SPEIs projecting substantially smaller increases in drought severity, frequency, duration, and impacted area, consistent with previous studies[18,34,35,41]. Furthermore, we find limited robust evidence for significant acceleration in drought trends under either Penman-type or energy-based SPEIs. Our results directly challenge a recent study[8] reporting warming-accelerated drought trends inferred mainly from comparing a short time period (2018–2022) with a longer one (1981–2017). Comparisons between arbitrarily selected time intervals are highly sensitive to interannual variability and suffer from the problem of "overstating statistical significance by 'cherry-picking' the location of the changepoint times"[46]. A different temporal segmentation with an equal time split (1981–2002 vs. 2003–2024) reveals clear deceleration in drought trends after 2003 (Supplementary Fig. 2).

Our calculation of acceleration as the rate of change in moving decadal trends is a more robust method, offering insights into different directions and rates of drought deterioration or recovery (Figs. 2 and 3). The decadal trends of both drought severity and drought-affected area indicate alternating patterns of drought deterioration and recovery across the past four decades for the majority of land areas, resulting in limited long-term (first-order) drying trends and no detectable signal of acceleration (second-order) in drought. This revised understanding of drought trends and acceleration is more consistent with observed increasing terrestrial ecosystem NPP and WUE, and aligns with other ecohydrological studies finding no projected expansion of global drylands under climate warming[42].

Detecting drought acceleration is inherently challenging due to internal climate variability and the reduction of effective degrees of freedom caused by temporal autocorrelation, particularly within overlapping 10-year moving windows. By employing the MMK test to explicitly account for this autocorrelation, our approach rigorously prevents the inflation of false positive (Type I) errors. Furthermore, a Monte Carlo power analysis (see the "Methods" section for details) based on the highly sensitive Penman-type SPEI (serving as a conservative stress test) reveals that an absolute acceleration of $\geq 0.002\ yr^{-2}$ is required to achieve an 80% detection power during the 1981–2024 period (Supplementary Fig. 22a). The observed global SPEI accelerations are an order of magnitude smaller (roughly -0.00022 to $0.00009\ yr^{-2}$) (Supplementary Fig. 10a), resulting in a minimal detection rate of ~1.2%. Rather than indicating a methodological flaw, this extremely low power reflects the rigorous robustness of our approach against false positive (Type I) errors, demonstrating that any actual acceleration is too marginal to emerge from natural climate variability. This analysis also highlights an interesting signal-to-noise trade-off: extending the record to 1950–2024 using ERA5-Land paradoxically doubles the detection threshold to $\sim 0.004\ yr^{-2}$ due to high uncertainties in pre-satellite era forcing (Supplementary Fig. 22b), which severely penalizes the statistical test and negates the benefit of a longer record (unlike the 124-year CRU record, where the threshold theoretically drops to $0.0005\ yr^{-2}$, Supplementary Fig. 22c). Thus, the 1981–2024 satellite-era data provides the optimal balance of data quality and statistical power, confirming that the lack of global drought acceleration is a robust reflection of physical reality rather than an artifact of a limited study period.

Our analysis reveals that drought assessment based on empirical meteorological drought indices such as SPEI is highly sensitive to the methodological choice of the underlying PET formulation. Penman-type, aerodynamics-dominated PETs systematically overestimate drought trends by treating relative humidity and VPD as externally prescribed, quasi-static variables, while neglecting dynamic land-atmosphere feedbacks under limited surface moisture availability[34] (Supplementary Fig. 1). In contrast, energy-based PET formulations explicitly capture land-atmosphere feedbacks[29,35,36]: when a dry land surface becomes wet, enhanced evaporation moistens the boundary layer, adjusting relative humidity, VPD, and the temperature gradient between the surface and overlying air, which constrains further increases in evapotranspiration (Supplementary Fig. 1). These feedbacks establish net radiation as the primary driver and constraint of evapotranspiration over land[35], which explains why energy-based PETs provide a more physically consistent representation of drought trends, particularly in arid and semi-arid regions[34–36]. This physical consistency is critical because while global warming has led to widespread increases in VPD[50], net radiation (the available energy for evaporation) does not increase proportionally with warming[29]. Given that PET primarily scales with surface net radiation rather than temperature or VPD, as demonstrated by multiple empirical and theoretical studies[30,33,35,51,52], energy-based formulations naturally yield only modest changes in global mean aridity or drought with warming, compared to the large increases by aerodynamics-dominated approaches that assume PET primarily scales with VPD[18,23,34,35]. These mechanistic differences explain why much of the reported global drought intensification by the widely-used Penman-type PETs stems from methodological bias[9,34,53] rather than reflecting the true magnitude of the underlying drying trend[42].

The large divergence between Penman- and energy-based drought metrics resonates with the so-called aridity paradox, whereby observed vegetation growth and ecosystem water status are inconsistent with the widespread drying trends inferred from Penman-type aridity or drought indices[29,34,36,44,54] (Supplementary Fig. 20). Independent lines of evidence, including continued global greening[55,56], increasing vegetation water-use efficiency[57], and paleoclimate records indicating limited land aridification during past warm periods[58], support the consistency of energy-based drought estimates. Elevated CO_2 allows plants to maintain photosynthesis with reduced stomatal conductance, improving WUE[57], while other adaptive traits, such as root adjustment and leaf orientation changes, further mitigate plant sensitivity to VPD[59]. Although both Penman-type and energy-based formulations incorporate net radiation as a fundamental driver, they diverge critically in their aerodynamic components. Penman-type methods treat the exponentially rising VPD and aerodynamic components as independent atmospheric forcings, allowing calculated evaporative demand to scale aggressively and often unrealistically exceed the actual available surface energy limit[23,40]. In contrast, energy-based PET formulations, although not directly capturing soil moisture constraints or explicit vegetation regulation[28], improve ecohydrological drought assessment by indirectly capturing the physical limits on stomatal exchange of water vapor and CO_2 imposed by surface energy availability[52,60,61] and land–atmosphere feedbacks[34]. By implicitly capturing the compensating effects of rising CO_2 and VPD on evaporative demand—as CO_2-induced reductions in transpiration alter the surface energy balance and feed back to constrain net radiation—energy-based approaches provide drought metrics that are more consistent with observed ecosystem responses[34]. This emphasizes that drought stress is ultimately experienced by ecosystems and shaped by vegetation physiological responses and ecohydrological feedbacks[29,54,62]. Some studies indicate that the direct CO_2 physiological effect on large-scale aridity trends is secondary relative to the dominant role of land–atmosphere coupling constraints on evaporation embedded in energy-based PETs[34–36]. Recognizing the limitations of Penman-type PET and adopting energy-based formulations in drought and aridity indices can largely resolve the ongoing debate surrounding the aridity paradox.

Drought trends exhibit pronounced spatial heterogeneity, with the differences between Penman-type and energy-based SPEIs being dependent on the background climate (Supplementary Figs. 3 and 5): in arid regions, Penman-type PETs severely overestimate evaporative demand and associated drought trends, whereas in humid regions, surface energy constraints moderate evaporative demand and minimize the methodological gap. This explains why the divergence between Penman- and energy-based drought metrics grows with increasing aridity. Importantly, these methodological differences are not limited to SPEI trend magnitude but also extend to trends in drought frequency and duration (Supplementary Figs. 18 and 19) and the temporal evolution of these trends (i.e., acceleration/deceleration, Fig. 3 and Supplementary Figs. 16 and 17). This spatial heterogeneity has important ecological and management implications, as overestimation of drought events in arid regions may misguide resource allocation. Integrating ecohydrological understanding with spatially explicit analyses, using a wealth of hydroclimatic observations and direct model outputs, could facilitate more accurate, physically consistent drought assessments across varying climate zones[41].

Beyond these spatial patterns, it is also important to emphasize that the absence of a statistically detectable acceleration does not mean that the severity of ongoing drought intensification has diminished. Both PET frameworks in this study consistently indicate a statistically significant, monotonic drying trend over 1981–2024 (Fig. 1), and even a steady, non-accelerating increase in drought severity and affected area can accumulate into substantial cumulative impacts on freshwater availability, ecosystem functioning, and food security over multi-decadal timescales[1–4]. While our finding that the rate of drought intensification is not itself increasing presents a less catastrophic trajectory than an accelerating one, it does not alter the fact that large areas of quasi-global land continue to experience a robust, ongoing drying trend that warrants sustained climate adaptation planning.

We also acknowledge the methodological nuances and inherent limitations of drought assessment across different contexts. While our findings highlight the inflation artifacts of Penman-type PETs under large-scale, water-limited conditions, these formulations are not inherently incorrect in all conditions. Penman-based SPEIs may be appropriate for agricultural drought monitoring in some circumstances, particularly over small irrigated areas or water bodies where surface conditions are decoupled from broader atmospheric feedbacks[63]. Conversely, in strictly arid environments, employing any PET-based metric has inherent limitations. In such regions, actual evapotranspiration is overwhelmingly governed by moisture supply rather than atmospheric demand; thus, further increases in PET do not necessarily translate to additional ecosystem water loss. Therefore, our results do not negate the utility of Penman-type metrics in all conceivable circumstances, but rather underscore the necessity of matching the chosen PET physics—whether aerodynamically sensitive (Penman-type) or physically bounded (energy-based)—to the specific spatial scale, aridity regime, and drought type. Consequently, as advocated by several pivotal studies[40,64,65], an alternative and perhaps preferable trajectory for the field is to move beyond offline PET-based metrics entirely. Future research should therefore increasingly prioritize direct or integrated ecohydrological indicators, such as dynamic soil moisture profiles[66], actual evapotranspiration, plant physiological stress metrics (e.g., sun-induced chlorophyll fluorescence, SIF), and combined ecohydrological indices[42,67] derived from coupled model outputs and direct observations, to more accurately capture ecosystem drought stress. Crucially, as our attribution analysis demonstrates that precipitation overwhelmingly dominates (75%) long-term drought trends under energy-based frameworks (Supplementary Fig. 6), constraining the inherent uncertainty in precipitation observations remains paramount for robust future hydroclimatic assessments. Our analysis also highlights the importance of employing statistically robust methods for detecting trend acceleration. Furthermore, spatially explicit analyses across climate zones and temporal scales will refine drought predictions and support targeted management of vulnerable ecosystems. Finally, actively reducing methodological uncertainties in drought metrics, such as those arising from PET formulation choices, and improving drought impact monitoring through the integration of direct ecohydrological observations and coupled model outputs will provide more reliable foundations for designing climate adaptation strategies, particularly for water resource management and agricultural planning in a warming world.

In summary, our findings demonstrate that the reported intensification of drought under recent global warming is greatly overstated when using Penman-type SPEIs. Notably, we find no detectable widespread acceleration in global drought, regardless of the PET formulations employed. Penman-type SPEIs overestimate drying trends across drought severity, frequency, duration, and affected area, particularly in water-limited regions, whereas energy-based approaches provide estimates more consistent with observed ecosystem responses, including increases in NPP and WUE. The systematic bias in Penman-type methods, combined with mounting evidence from ecosystem observations and advances in land-atmosphere coupling theory, underscores the urgency of transitioning traditional drought monitoring frameworks toward energy-based formulations that better reflect physical and biological realities.

Methods

Drought index

A widely utilized drought index, the SPEI, which incorporates both precipitation and atmospheric evaporative demand (PET), was employed to evaluate global drought severity. The SPEI is computed by standardizing the precipitation-minus-PET difference through a log-logistic distribution, with its parameters (α, β, γ) estimated by the L-moment method, to ensure spatiotemporal comparability. We employed the entire period from 1981 to 2024 as the baseline for SPEI calculation to capture the full variability inherent in the input data. SPEI was computed using the R package available on GitHub at https://github.com/sbegueria/SPEI/.

PET was estimated using six distinct methods: Penman[25] (abbreviated as PE), Penman–Monteith for reference crop[32] (abbreviated as PM-RC), Penman for open water[31] (abbreviated as PE-OW), and the methods of Zhou and Yu[28] (abbreviated as ZY), Yang and Roderick[29] (abbreviated as YR), and Milly and Dunne[23] (abbreviated as MD).

The reference crop (FAO-56) Penman–Monteith (PET_{PM-RC}) equation represents PET from a standardized, well-watered reference vegetation surface, typically defined as a short grass canopy with fixed aerodynamic and surface resistances. By prescribing constant canopy characteristics and assuming non-limiting soil moisture conditions, this formulation isolates the atmospheric evaporative demand under a reference land-surface state. As a result, it provides a widely used benchmark for assessing climatic controls on evapotranspiration while minimizing the influence of site-specific vegetation properties. The Penman–Monteith equation for reference crop (PET_{PM-RC}, mm day^{-1}) is given by

$$PET_{PM-RC} = \frac{0.408\Delta_a\left(R_n - G\right) + \gamma_s \frac{900}{T_a+273} u_2 (e_s - e_a)}{\Delta_a + \gamma_s(1 + 0.34u_2)} \tag{1}$$

where R_n is net radiation (MJ m^{-2} day^{-1}), G is the surface heat flux (MJ m^{-2} day^{-1}), u_2 is the wind speed at 2 m height (m s^{-1}), γ_s is the psychrometric constant (kPa °C^{-1}), Δ_a is the slope of the saturated vapor pressure as a function of air temperature (kPa °C^{-1}), T_a is the air temperature at 2 m height (°C), e_s is the saturation vapor pressure at T_a (kPa) and e_a is the actual vapor pressure at dew point temperature (T_d) (kPa).

The slope of the saturated vapor pressure curve (Δ_a) (kPa °C^{-1}) as a function of T_a is given by

$$\Delta_a = \frac{4098 \cdot e_s}{(T_a + 237.3)^2} \tag{2}$$

The psychrometric constant (γ_s, kPa °C^{-1}) is calculated as

$$\gamma_s = \frac{c_p \cdot P_s}{\lambda_s \cdot \varepsilon} \tag{3}$$

where c_p is the specific heat of the air at constant pressure (0.00101 MJ kg^{-1} °C^{-1}), P_s is the surface pressure (kPa), ε is the molecular weight ratio of water vapor to dry air (typically 0.622), λ_s is the latent heat of vaporization (MJ kg^{-1}), evaluated at surface temperature (T_s) and expressed as a function of T_s, such that the psychrometric constant γ_s is consistently evaluated at T_s, in line with the energy-balance perspective adopted in the energy-based PET formulations.

$$\lambda_s = 2.501 - 0.002361 \times T_s \tag{4}$$

The saturation vapor pressure (e_s, kPa) based on air temperature (T_a, °C) is calculated as

$$e_s = 0.6108 \cdot e^{\frac{17.27 \cdot T_a}{T_a + 237.3}} \tag{5}$$

The actual vapor pressure (e_a, kPa) based on dew point temperature (T_d, °C) is derived as

$$e_a = 0.6108 \cdot e^{\frac{17.27 \cdot T_d}{T_d + 237.3}} \tag{6}$$

Penman PET for open water (PET_{PE-OW}, mm·day^{-1}) is calculated as

$$PET_{PE-OW} = \frac{\Delta_a (R_n - G) + 6.43(1 + 0.536 u_2)\gamma_s (e_s - e_a)}{\lambda_s (\Delta_a + \gamma_s)} \tag{7}$$

All variables in Eq. (7) are defined as above.

Since the calculation of aerodynamic conductance requires tree height data, which is not provided in the four precipitation and meteorological datasets we used, and considering the uncertainty associated with this calculation of aerodynamic conductance, we adopted the Penman-type PET provided by the GLEAM dataset[68] based on MSWEX100 forcing. As a result, the Penman formulation within the Penman-type PET class is represented by a single data source in our analysis, whereas all other PET formulations are evaluated using two independent forcing datasets. The detailed PET calculation formula based on Penman method from GLEAM dataset is as follows:

$$PET_{PE} = \frac{\Delta_a (R_n - G) + \rho_a c_p g_a (e_s - e_a)}{\lambda_a (\Delta_a + \gamma_a)} \tag{8}$$

where ρ_a is the air density (kg m^{-3}), g_a is the bulk aerodynamic conductance (m day^{-1}), γ_a is the psychrometric constant (kPa °C^{-1}) evaluated at air temperature, is calculated as

$$\gamma_a = \frac{c_p \cdot P_s}{\lambda_a \cdot \varepsilon} \tag{9}$$

where λ_a is the latent heat of vaporization (MJ kg^{-1}), expressed as a function of air temperature (T_a, °C):

$$\lambda_a = 2.501 - 0.002361 \times T_a \tag{10}$$

All other variables in Eq. (9) are defined as in the previous equations.

Energy-based PET formulations are rooted in the fundamental constraint imposed by surface energy availability. In the classical Budyko framework[61], PET is commonly approximated as being proportional to net radiation (R_n) under wet conditions, where evapotranspiration is primarily energy-limited. In practice, however, PET does not scale perfectly with R_n, as a fraction of available energy is dissipated as sensible heat and other fluxes even under non-water-stressed conditions. To account for these departures from the idealized energy limit, a variety of empirical energy-based PET formulations have been proposed[23,28–30]. The most recent energy-based PET (PET_e) builds on the estimation of the Bowen ratio in wet conditions (β_w)[28]:

$$PET_e = \frac{1}{1 + \beta_w} \frac{R_n}{\lambda_s} \tag{11}$$

where β_w denotes the actual Bowen ratio. Yang and Roderick[29] proposed a wet surface β_{w_Yang} (Eq. (11)) and optimized for saturated surfaces such as oceans, which captures the subtle variations in energy partitioning under wet conditions. Similarly, Zhou and Yu[28] revised β_w and showed that the PET_e based on β_{w_Zhou} (Eq. (12)) estimated under dry conditions can approximate actual ET accurately when the surface becomes saturated.

The wet surface Bowen ratios β_{w_Yang} and β_{w_Zhou} can be estimated by the following equations:

$$\beta_{w\_Yang} = 0.24 \frac{\gamma_s}{\Delta_s} \tag{12}$$

$$\beta_{w\_Zhou} = \frac{\gamma_s (T_s - T_a)}{(e_s^* - e_a)} \tag{13}$$

To avoid unrealistic values, β_{w_Zhou} calculated using Eq. (13) was constrained within physically reasonable bounds following Zhou and Yu[28]. Specifically, for each month, if $\beta_{w\_Zhou} < \beta_{w\_Yang}$, β_{w_Zhou} was set to β_{w_Yang}; if $\beta_{w\_Zhou} > \beta$, β_{w_Zhou}, was set to the actual Bowen ratio (β, the ratio of sensible over latent heat)[18]. Here, γ_s is the psychrometric constant (kPa °C^{-1}), calculated using Eq. (3). The slope of the saturated vapor pressure curve (Δ_s, kPa °C^{-1}) as a function of T_s is given by

$$\Delta_s = \frac{4098 \cdot e_s^*}{(T_s + 237.3)^2} \tag{14}$$

The saturation vapor pressure (e_s^*, kPa) based on surface temperature is calculated as

$$e_s^* = 0.6108 \cdot e^{\frac{17.27 \cdot T_s}{T_s + 237.3}} \tag{15}$$

Following Milly and Dunne (2016)[23], we adopt an energy-only PET formulation, in which PET is constrained solely by surface available energy. Energy-only PET is approximated as:

$$PET = 0.8 * \frac{R_n - G}{\lambda_s} \tag{16}$$

All variables in Eq. (16) are defined as above. At the monthly timescale considered here, ground heat flux (G) is generally small relative to the net radiation term and is thus neglected ($G = 0$) in all PET formulations presented above.

To rigorously assess the structural uncertainty of PET formulations and evaluate the influence of explicit land–atmosphere interactions, we incorporated two recently developed diagnostic models into our sensitivity analysis. First, we utilized the coupled formulation by Kim et al. (2023)[36], which explicitly constrains PET under a warming climate by incorporating actual atmospheric relative humidity and surface energy balance. To maintain physical consistency with the boundary layer energy state, this model is formulated within the specific humidity system:

$$\lambda_s PET_{Kim} = \frac{2RH_a s + \gamma_{sh}}{2RH_a s + 2\gamma_{sh}} (R_n - G) \tag{17}$$

where PET_{Kim} represents the evapotranspiration rate (mm day^{-1}); RH_a represents the relative humidity of the atmospheric state near the land surface (dimensionless fraction); s is the slope of the saturation specific humidity curve (kg kg^{-1} °C^{-1}); and γ_{sh} is the psychrometric constant in the specific humidity system (kg kg^{-1} °C^{-1}). The slope s is defined as the derivative of saturation specific humidity (q^*) with respect to temperature (T):

$$s = \frac{dq^*}{dT_a}, \ \gamma_{sh} = \gamma_a \frac{dq^*}{de_s^*} \tag{18}$$

where dq^* is derived from the saturation vapor pressure and atmospheric pressure (P_s) and the psychrometric constant γ_{sh} is derived by converting the standard psychrometric constant (γ_a, in kPa °C^{-1}) into the specific humidity framework. Crucially, the latent heat of vaporization (λ_s) and the psychrometric constant (γ_{sh}) are parameterized using the surface skin temperature (T_s) to reflect the energy state at the evaporating surface, while the slope s is determined by the air temperature (T_a). This approach explicitly accounts for the distinct thermal states and moisture capacities of the land surface and the overlying atmosphere. All other variables remain as defined above.

Second, we evaluated a simplified diagnostic physical model of soil moisture (Gallagher and McColl, 2025[48]), which derives near-surface soil saturation solely as a function of precipitation and net radiation:

$$s(t) = \frac{P(t)}{0.8\frac{R_n(t)}{\lambda_s} + P(t)} \tag{19}$$

where $s(t)$ represents the diagnostic near-surface soil saturation limit (a dimensionless fraction between 0 and 1); $P(t)$ is the precipitation rate (mm day^{-1}). By explicitly dividing surface net radiation $R_n(t)$ by the latent heat of vaporization λ_s, the energy term is properly converted to a water equivalent depth (mm day^{-1}) to ensure dimensional consistency with $P(t)$. All variables are evaluated at time step t.

Datasets

Two meteorological datasets, ERA5-Land[69] and MSWX100[70], were employed to calculate the PET, with six PET methods (PE, PE-OW, PM-RC, MD, YR, ZY) applied to MSWX100 and five PET methods (PE-OW, PM-RC, MD, YR, ZY) applied to ERA5-Land, yielding 11 distinct PET datasets. The PET dataset derived from MSWX100 climate data with the Penman (PE) method was directly downloaded from GLEAM[68] (https://www.gleam.eu/). However, the PE method was not applied to ERA5-Land due to the difficulty in obtaining precise and temporally continuous gridded aerodynamic conductance (g_a in Eq. (8)) over the entire study period (1981–2024). Although tree height data are available from satellite observations, these products typically have a short temporal span that fails to cover the earlier decades of our study. Furthermore, cross-sensor transitions (e.g., around the year 2000) and spatial discontinuities in these remote sensing products introduce substantial uncertainties into the g_a calculation. When calculating PETs with the MSWX100 dataset, a limited number of meteorological variables (e.g., sensible heat flux, latent heat flux, and skin temperature) were missing. These data gaps were filled using the corresponding records from the ERA5-Land dataset. Specifically, net radiation was derived based on the surface energy balance using these corresponding sensible and latent heat fluxes. Utilizing two precipitation datasets from MSWEP[71] and CHIRPS[72], we calculated SPEIs with two precipitation and PET combinations: (1) MSWEP_MSWX100, which includes six SPEI datasets based on MSWEP precipitation and six PETs from MSWX100, and (2) CHIRPS_ERA5-Land, which includes five SPEI datasets based on CHIRPS precipitation and five PETs from ERA5-Land. These pairings were specifically chosen to ensure internal consistency and physical coherence between precipitation and meteorological forcing, as each pair originates from the same or closely integrated data systems (i.e., the multi-source family for MSWEP/MSWX100, and the ERA5-based framework for CHIRPS/ERA5-Land). This approach avoids potential uncertainties or artificial biases that might arise from cross-combining unrelated data sources. For analysis and visualization, we grouped these 11 SPEIs by 6 PET methods, with each method representing the ensemble mean SPEI of two datasets (MSWEP_MSWX100 and CHIRPS_ERA5-Land), except for the PE method, which is the SPEI based on a single dataset (MSWEP_MSWX100). Furthermore, to provide auxiliary mechanistic validation, two advanced diagnostic models (Kim et al., 2023[36]; Gallagher and McColl, 2025[48]) were also applied to these same two data combinations and evaluated as an ensemble mean. These specific models were selected because they offer an independent physical benchmark by explicitly constraining evaporative demand through land-atmosphere coupling and atmospheric humidity feedbacks. Details of data used in this study are in Supplementary Table 3. Monthly data from all meteorological datasets were used in this study. These datasets were spatially aligned to a consistent 0.1° × 0.1° (latitude 1801, longitude 3600) resolution through bilinear interpolation using the climate data operators (CDO). All subsequent data processing, statistical analyses, and visualizations were performed in Python (version 3.8.18).

To ensure our findings regarding drought acceleration are not merely an artifact of the relatively short 1981–2024 period, we extended our analysis to provide a longer-term historical context. First, we utilized the ERA5-Land reanalysis dataset to evaluate long-term trends over the 1950–2024 period across the five available PET formulations (PE-OW, PM-RC, MD, YR, ZY). Second, we incorporated the Climatic Research Unit (CRU) Time-Series (TS) dataset (v4.09)[73] to assess drought dynamics over the 124-year period from 1901 to 2024, utilizing its native PM-RC PET formulation. Both extended datasets were subjected to the same spatial masking and aggregation protocols to ensure methodological consistency when comparing long-term historical accelerations. To ensure consistency with the spatial coverage of the CHIRPS dataset, the quasi-global mean SPEI time series for trend analysis was computed exclusively over the 50°N–50°S land areas, after applying a mask to exclude regions with an average annual precipitation below 180 mm. This hyper-arid threshold was applied because, in such environments, precipitation is persistently dwarfed by atmospheric evaporative demand, leading to a strictly PET-dominated water balance. Under these conditions, the probability distribution fitting required for SPEI standardization becomes statistically unstable due to highly skewed and nearly zero-inflated precipitation inputs. Consequently, SPEI values in these regions lose their sensitivity to actual interannual hydroclimatic variability and are instead disproportionately driven by methodological differences in PET estimations. The precipitation mask was generated separately for each dataset, based on the precipitation data used to calculate the corresponding SPEI.

To evaluate ecosystem responses to drought, we used global monthly net primary productivity (NPP) data from the GLASS remote sensing dataset[74] (0.05° resolution, 1981–2018; https://glass.hku.hk/download.html), which is derived from MODIS NPP products. Monthly transpiration (T) data were obtained from the GLEAM dataset (0.1° resolution)[68] (https://www.gleam.eu/). We calculated WUE as the ratio of NPP to T for each grid cell and month (WUE = NPP/T). Temporal trends in NPP and WUE were then analyzed to assess changes in ecosystem productivity and WUE over the study period (Supplementary Fig. 20).

Sen's slope analysis and significance test

The long-term trends in SPEI were analyzed using the non-parametric Mann–Kendall test and Sen's slope estimator. For each pixel, the Mann–Kendall test detects the statistical significance of monotonic trends, while Sen's slope estimator quantifies the magnitude of change by computing the median of all pairwise slopes. This combined approach provides a robust measure of trend direction and rate, resistant to outliers and non-normal data distributions.

Detecting drought acceleration is inherently challenging due to internal climate variability and the reduction of effective degrees of freedom caused by temporal autocorrelation, which becomes especially critical when analyzing highly autocorrelated overlapping 10-year moving windows. To explicitly address these statistical challenges, our trend detection pipeline employed the MMK test[75]. This method estimates the lag-1 autocorrelation of the detrended series and rigorously adjusts the variance of the Mann–Kendall statistic using a variance correction factor based on the effective degrees of freedom. By doing so, it robustly accounts for temporal autocorrelation and prevents the inflation of Type I errors (false positives) during both the long-term trend and acceleration assessments.

Statistical comparison of decadal trend distributions

To rigorously evaluate whether the decadal-trend series derived from Penman-type and energy-based formulations actually differ in their overall distributions (as opposed to merely displaying different ensemble-mean slopes), we implemented three complementary statistical metrics to compare the 35 matched 10-year moving windows: (1) to leverage the naturally paired structure of the data (i.e., comparing the two formulations within each matched 10-year window), we applied the non-parametric Wilcoxon signed-rank test. This test evaluates whether there is a consistent, directional median shift between the paired decadal-trend values; (2) we employed the two-sample Kolmogorov–Smirnov (KS) test, a non-parametric test designed to detect differences in the overall shape, scale, and location of the two empirical trend distributions without relying on their paired structure; and (3) to quantitatively estimate the empirical overlap of the two trend distributions, we calculated the distribution overlap coefficient (OVL) based on kernel density estimation (KDE) with a Gaussian kernel. The OVL ranges from 0 (complete separation of distributions) to 1 (perfectly identical distributions) and is computed as

$$OVL = \int \min(f_{PE}(x), f_{Rn}(x))dx) \tag{19}$$

where $f_{\mathrm{PE}}(x)$ and $f_{\mathrm{Rn}}(x)$ represent the estimated probability density functions of the decadal trends for the Penman-type and energy-based groups, respectively.

Contribution analysis

This study employs a climatology-based attribution framework to quantitatively assess the relative contributions of PET and precipitation to long-term SPEI trends. The calculation procedure is as follows: (1) we calculate the decadal SPEI trends (1981–2024) using the non-parametric Theil–Sen estimator under three scenarios: a "true observational" scenario using transient monthly time series for both variables; a "PET climatology" scenario where PET is fixed to its long-term multi-year monthly average while precipitation remains transient; and a "precipitation climatology" scenario fixing precipitation to its climatology while retaining the transient PET time series; (2) isolation of absolute contributions: the absolute contribution of a single climate variable is defined as the absolute difference between the trend of the observational scenario and the trend of the scenario where that specific variable is held at its climatology. For instance, the absolute contribution of precipitation is the absolute difference between the observed trend and the precipitation climatology trend; the PET contribution is calculated similarly; and (3) quantification of relative percentages: the relative percentage contribution of each factor is determined by dividing its absolute contribution by the sum of the absolute contributions from both variables.

Definition and classification of drought acceleration

Drought acceleration was quantified as the temporal change in the rate of SPEI trends. Specifically, the first-order trend represents the linear trend in SPEI over the study period, indicating whether drought conditions are intensifying or alleviating. The second-order trend, hereafter referred to as acceleration, is defined as the linear trend of the decadal SPEI trends, describing whether the rate of SPEI change increases or decreases over time. To facilitate physical interpretation, the sign of acceleration was interpreted jointly with the sign of the first-order SPEI trend, resulting in four distinct drought-evolution categories (Supplementary Table 2). The first-order SPEI trend was evaluated over the full study period to represent the long-term drought tendency, whereas acceleration was derived from the temporal evolution of sliding decadal SPEI trends. This separation allows the long-term drought state to be distinguished from changes in the rate of drought evolution, thereby avoiding conceptual mixing between trend direction and trend acceleration.

For the quasi-global time-series analysis (Fig. 2), both Penman-type and energy-based SPEIs exhibit negative first-order trends, indicating an overall drought intensification during the study period. Because SPEI is an inverse indicator of drought (where negative values and negative trends denote drier conditions), the mathematical sign of the second-order trend (acceleration) must be interpreted relative to this negative baseline. Under this common background, the sign of acceleration directly reflects changes in the rate of drought intensification: a positive second-order trend denotes a deceleration of drought intensification, whereas a negative second-order trend indicates that drought intensification is accelerating.

Calculation of drought duration and frequency

In addition to the long-term trends in SPEI, we evaluated trends in drought duration and frequency. Drought duration is defined as the annual maximum length of consecutive months with SPEI < -1, while drought frequency is defined as the annual total number of months with SPEI < -1. To prevent statistical artifacts caused by the sparsity of monthly drought occurrences, the trend calculations were performed on these temporally aggregated annual metrics rather than monthly binary arrays. Furthermore, the reliance on the non-parametric Theil–Sen estimator ensures that the derived slopes are highly robust against outliers and the skewed data distributions inherent to discrete extreme events.

Statistical power analysis for acceleration detection

To evaluate the statistical power of our acceleration detection framework and determine the minimum magnitude of trend rate changes required to emerge from background climate noise, we conducted a Monte Carlo power analysis. First, we estimated the empirical noise parameters (standard deviation and lag-1 autocorrelation) from the detrended residuals of the actual area-weighted SPEI series. We specifically utilized the Penman-type SPEI series (and the corresponding SPEI derived from PM-RC PET formulation for the 1901–2024 CRU dataset) for this estimation, as they exhibit the highest variance and sensitivity to warming, thereby providing a conservative "worst-case" stress test for our detection framework. We then generated 500 synthetic time series by superimposing a range of predefined acceleration signals (from 0 to 0.005 yr^{-2}) onto the baseline linear trend, integrated with the empirically derived first-order autoregressive process (AR(1)) red noise. Each synthetic series was subjected to our exact analytical pipeline (10-year overlapping windows followed by the MMK test). The statistical power for each magnitude was calculated as the detection rate ($P < 0.05$) across the 500 simulations, which allowed us to identify the theoretical minimum detectable acceleration threshold required to achieve an 80% power. This analysis was independently conducted for the satellite era (1981–2024) and the extended historical records (1950–2024 for ERA5-Land and 1901–2024 for CRU) to explicitly evaluate the signal-to-noise trade-offs associated with different temporal record lengths.

Data availability

All data described in the main text are publicly available. The ERA5-Land data are available from the European Centre for Medium-Range Weather Forecasts (ECMWF) at https://cds.climate.copernicus.eu/datasets/reanalysis-era5-land-monthly-means?tab=overview. The MSWX100 data can be accessed through the GloH2O platform at https://www.gloh2o.org/mswx/. The CHIRPS precipitation data (V2) is distributed by the Climate Hazards Group at https://www.chc.ucsb.edu/data/chirps/. The MSWEP precipitation dataset is available from the GloH2O website at https://www.gloh2o.org/mswep/. The CRU TS v4.09 data were obtained from the Climatic Research Unit, University of East Anglia, at https://crudata.uea.ac.uk/cru/data/hrg/cru_ts_4.09/. Global Land Evaporation Amsterdam Model (GLEAM) v4.2a datasets are available at https://www.gleam.eu/. The Global Land Surface Satellite (GLASS) NPP product was obtained from the University of Hong Kong at https://glass.hku.hk/download.html.

Code availability

The intermediate data and code for replicating the figures and analysis have been deposited in the Zenodo repository (https://zenodo.org/records/20455711)[76].

Received: 11 February 2026; Accepted: 11 August 2026;
Published online: 11 September 2026

References

1. Anderegg, W. R. L. et al. Hydraulic diversity of forests regulates ecosystem resilience during drought. *Nature* **561**, 538–541 (2018).
2. Schwalm, C. R. et al. Global patterns of drought recovery. *Nature* **548**, 202–205 (2017).
3. Xu, C. et al. Increasing impacts of extreme droughts on vegetation productivity under climate change. *Nat. Clim. Change* **9**, 948–953 (2019).

4. Zhou, S., Zhang, Y., Williams, A. & Gentine, P. Projected increases in intensity, frequency, and terrestrial carbon costs of compound drought and aridity events. *Sci. Adv.* **5**, eaau5740 (2019).
5. Trenberth, K. E. et al. Global warming and changes in drought. *Nat. Clim. Change* **4**, 17–22 (2013).
6. Zaitchik, B. F., Rodell, M., Biasutti, M. & Seneviratne, S. I. Wetting and drying trends under climate change. *Nat. Water* **1**, 502–513 (2023).
7. Lian, X. et al. Multifaceted characteristics of dryland aridity changes in a warming world. *Nat. Rev. Earth Environ.* **2**, 232–250 (2021).
8. Gebrechorkos, S. H. et al. Warming accelerates global drought severity. *Nature* **642**, 628–635 (2025).
9. Dai, A. Increasing drought under global warming in observations and models. *Nat. Clim. Change* **3**, 52–58 (2012).
10. Dai, A. Drought under global warming: a review. *WIREs Clim. Change* **2**, 45–65 (2011).
11. Jiao, W. et al. Observed increasing water constraint on vegetation growth over the last three decades. *Nat. Commun.* **12**, 3777 (2021).
12. Greve, P. et al. Global assessment of trends in wetting and drying over land. *Nat. Geosci.* **7**, 716–721 (2014).
13. Chiang, F., Mazdiyasni, O. & AghaKouchak, A. Evidence of anthropogenic impacts on global drought frequency, duration, and intensity. *Nat. Commun.* **12**, https://doi.org/10.1038/s41467-021-22314-w (2021).
14. Williams, A. P. et al. Large contribution from anthropogenic warming to an emerging North American megadrought. *Science* **368**, 314–318 (2020).
15. Rodell, M. & Li, B. Changing intensity of hydroclimatic extreme events revealed by GRACE and GRACE-FO. *Nat. Water* **1**, 241–248 (2023).
16. Gudmundsson, L. et al. Globally observed trends in mean and extreme river flow attributed to climate change. *Science* **371**, 1159–1162 (2021).
17. Tegos, A., Stefanidis, S., Cody, J. & Koutsoyiannis, D. On the Sensitivity of standardized-precipitation-evapotranspiration and aridity indexes using alternative potential evapotranspiration models. *Hydrology* **10**, 64 (2023).
18. Zhou, S. & Yu, B. Reconciling the discrepancy in projected global dryland expansion in a warming world. *Global Change Biol.* **31**, https://doi.org/10.1111/gcb.70102 (2025).
19. Vicente-Serrano, S. M., Van der Schrier, G., Beguería, S., Azorin-Molina, C. & Lopez-Moreno, J.-I. Contribution of precipitation and reference evapotranspiration to drought indices under different climates. *J. Hydrol.* **526**, 42–54 (2015).
20. Liu, W. et al. Impact of the potential evapotranspiration models on drought monitoring. *J. Hydrol.: Reg. Stud.* **58**, 102236 (2025).
21. Foster, G. & Rahmstorf, S. Global warming has accelerated significantly. *Geophys. Res. Lett.* **53**, https://doi.org/10.1029/2025gl118804 (2026).
22. Seneviratne, S. I. et al. in *Climate Change 2021 – The Physical Science Basis* Ch. 11, 1513–1766 (Cambridge University Press, 2021).
23. Milly, P. C. D. & Dunne, K. A. Potential evapotranspiration and continental drying. *Nat. Clim. Change* **6**, 946–949 (2016).
24. Karimzadeh, S., Ahmadi, A., Baldocchi, D. & Fisher, J. B. Climate change has increased global evaporative demand except in South Asia. *Commun. Earth Environ.* **6**, 1009 (2025).
25. Penman, H. L. & Keen, B. A. Natural evaporation from open water, bare soil and grass. *Proc. R. Soc. Lond. Ser. A Math. Phys. Sci.* **193**, 120–145 (1948).
26. Monteith, J. L. Evaporation and environment. *Symposia Soc. Exp. Biol.* **19**, 205–234 (1965).
27. Thornthwaite, C. W. An approach toward a rational classification of climate. *Geogr. Rev.* **38**, 55–94 (1948).
28. Zhou, S. & Yu, B. Physical basis of the potential evapotranspiration and its estimation over land. *J. Hydrol.* **641**, https://doi.org/10.1016/j.jhydrol.2024.131825 (2024).
29. Yang, Y. & Roderick, M. L. Radiation, surface temperature and evaporation over wet surfaces. *Q. J. R. Meteorol. Soc.* **145**, 1118–1129 (2019).
30. Greve, P., Roderick, M. L., Ukkola, A. M. & Wada, Y. The aridity Index under global warming. *Environ. Res. Lett.* **14**, https://doi.org/10.1088/1748-9326/ab5046 (2019).
31. Stedinger, J., Vogel, R., Foufoula-Georgiou, E. & Maidment, D. R. *Handbook of Hydrology* (McGraw-Hill, Inc., 1993).
32. Allen, G. R., Pereira, S. L., Raes, D. & Smith, M. *Crop Evapotranspiration—Guidelines for Computing Crop Water Requirements*. *FAO Irrigation and drainage paper 56*, *Rome*, http://www.fao.org/docrep/X0490E/X0490E00.htm (1998).
33. Maes, W. H., Gentine, P., Verhoest, N. E. C. & Miralles, D. G. Potential evaporation at eddy-covariance sites across the globe. *Hydrol. Earth Syst. Sci.* **23**, 925–948 (2019).
34. Zhou, S. & Yu, B. Neglecting land–atmosphere feedbacks overestimates climate-driven increases in evapotranspiration. *Nat. Clim. Change* **15**, 1099–1106 (2025).
35. Tang, L. I. & McColl, K. A. Radiative-convective equilibrium over an idealized land surface with fixed soil moisture. *J. Clim.* https://doi.org/10.1175/jcli-d-24-0438.1 (2025).
36. Kim, Y., Garcia, M. & Johnson, M. S. Land–atmosphere coupling constrains increases to potential evaporation in a warming climate: implications at local and global scales. *Earth's Futur.* **11**, https://doi.org/10.1029/2022ef002886 (2023).
37. Byrne, M. P. et al. Theory and the future of land-climate science. *Nat. Geosci.* **17**, 1079–1086 (2024).
38. Gentine, P. et al. Coupling between the terrestrial carbon and water cycles—a review. *Environ. Res. Lett.* **14**, https://doi.org/10.1088/1748-9326/ab22d6 (2019).
39. Zhou, S. et al. Soil moisture–atmosphere feedbacks mitigate declining water availability in drylands. *Nat. Clim. Change* **11**, 38–44 (2021).
40. Roderick, M. L., Greve, P. & Farquhar, G. D. On the assessment of aridity with changes in atmospheric CO_2. *Water Resour. Res.* **51**, 5450–5463 (2015).
41. McColl, K. A., Roderick, M. L., Berg, A. & Scheff, J. The terrestrial water cycle in a warming world. *Nat. Clim. Change* **12**, 604–606 (2022).
42. Berg, A. & McColl, K. A. No projected global drylands expansion under greenhouse warming. *Nat. Clim. Change* **11**, 331–337 (2021).
43. He, B., Wang, S., Guo, L. & Wu, X. Aridity change and its correlation with greening over drylands. *Agric. For. Meteorol.* **278**, 107663 (2019).
44. Scheff, J., Mankin, J. S., Coats, S. & Liu, H. CO_2-plant effects do not account for the gap between dryness indices and projected dryness impacts in CMIP6 or CMIP5. *Environ. Res. Lett.* **16**, 034018 (2021).
45. Scheff, J., Coats, S. & Laguë, M. M. Why do the global warming responses of land-surface models and climatic dryness metrics disagree? *Earth's. Future* **10**, e2022EF002814 (2022).
46. Beaulieu, C., Gallagher, C., Killick, R., Lund, R. & Shi, X. A recent surge in global warming is not detectable yet. *Commun. Earth Environ.* **5**, 576 (2024).
47. Seo, K.-W. et al. Abrupt sea level rise and Earth's gradual pole shift reveal permanent hydrological regime changes in the 21st century. *Science* **387**, 1408–1413 (2025).
48. Gallagher, T. & McColl, K. A. Climate-scale variability in soil moisture explained by a simple theory. *Geophys. Res. Lett.* **52**, https://doi.org/10.1029/2025gl115044 (2025).
49. Kondo, M. et al. Land use change and El Nino-Southern Oscillation drive decadal carbon balance shifts in Southeast Asia. *Nat. Commun.* **9**, 1154 (2018).
50. Sherwood, S. & Fu, Q. A drier future? *Science* **343**, 737–739 (2014).
51. Kleidon, A. *Thermodynamic Foundations of the Earth System* (Cambridge University Press, 2016).
52. Kleidon, A. What limits photosynthesis? Identifying the thermodynamic constraints of the terrestrial biosphere within the Earth system. *Biochim. Biophys. Acta Bioenerg.* **1862**, 148303 (2021).

53. Feng, S. & Fu, Q. Expansion of global drylands under a warming climate. *Atmos. Chem. Phys.* **13**, 10081–10094 (2013).
54. Yang, Y., Roderick, M. L., Zhang, S., McVicar, T. R. & Donohue, R. J. Hydrologic implications of vegetation response to elevated CO_2 in climate projections. *Nat. Clim. Change* **9**, 44–48 (2019).
55. Zhu, Z. et al. Greening of the Earth and its drivers. *Nat. Clim. Change* **6**, 791–795 (2016).
56. Piao, S. et al. Characteristics, drivers and feedbacks of global greening. *Nat. Rev. Earth Environ.* **1**, 14–27 (2019).
57. Peng, J. et al. Evidence for the acclimation of ecosystem photosynthesis to soil moisture. *Nat. Commun.* **15**, 9795 (2024).
58. McGee, D., deMenocal, P. B., Winckler, G., Stuut, J. B. W. & Bradtmiller, L. I. The magnitude, timing and abruptness of changes in North African dust deposition over the last 20,000yr. *Earth Planet. Sci. Lett.* **371-372**, 163–176 (2013).
59. Grossiord, C. et al. Plant responses to rising vapor pressure deficit. *N. Phytol.* **226**, 1550–1566 (2020).
60. Priestley, C. H. B. & Taylor, R. J. On the assessment of surface heat flux and evaporation using large scale parameters. *Mon. Weather Rev.* **100**, 81–92 (1972).
61. Budyko, M. I. *Climate and Life* (Academic Press, 1974).
62. Kannenberg, S., Anderegg, W., Barnes, M., Dannenberg, M. & Knapp, A. Dominant role of soil moisture in mediating carbon and water fluxes in dryland ecosystems. *Nat. Geosci.* **17**, 1–6 (2024).
63. Beguería, S., Vicente-Serrano, S. M., Reig, F. & Latorre, B. Standardized precipitation evapotranspiration index (SPEI) revisited: parameter fitting, evapotranspiration models, tools, datasets and drought monitoring. *Int. J. Climatol.* **34**, 3001–3023 (2014).
64. Swann, A. L., Hoffman, F. M., Koven, C. D. & Randerson, J. T. Plant responses to increasing CO_2 reduce estimates of climate impacts on drought severity. *Proc. Natl. Acad. Sci. USA* **113**, 10019–10024 (2016).
65. Lemordant, L., Gentine, P., Swann, A. S., Cook, B. I. & Scheff, J. Critical impact of vegetation physiology on the continental hydrologic cycle in response to increasing CO(2). *Proc. Natl. Acad. Sci. USA* **115**, 4093–4098 (2018).
66. Fu, Z. et al. Critical soil moisture thresholds of plant water stress in terrestrial ecosystems. *Sci. Adv.* **8**, eabq7827 (2022).
67. Chang, Q. et al. Earlier ecological drought detection by involving the interaction of phenology and eco-physiological function. *Earth's Futur.* **11**, https://doi.org/10.1029/2022ef002667 (2023).
68. Miralles, D. G. et al. GLEAM4: global land evaporation and soil moisture dataset at 0.1° resolution from 1980 to near present. *Sci. Data* **12**, https://doi.org/10.1038/s41597-025-04610-y (2025).
69. Muñoz-Sabater, J. et al. ERA5-Land: a state-of-the-art global reanalysis dataset for land applications. *Earth Syst. Sci. Data* **13**, 4349–4383 (2021).
70. Beck, H. et al. MSWX: global 3-hourly 0.1 bias-corrected meteorological data including near-real-time updates and forecast ensembles. *Bull. Am. Meteorol. Soc.* **103**, E710–E732 (2022).
71. Beck, H. et al. MSWEP V2 global 3-hourly 0.1° precipitation: methodology and quantitative assessment. *Bull. Am. Meteorol. Soc.* **100**, 473–500 (2018).
72. Funk, C. et al. The climate hazards infrared precipitation with stations—a new environmental record for monitoring extremes. *Sci. Data* **2**, 150066 (2015).
73. Harris, I., Osborn, T. J., Jones, P. & Lister, D. Version 4 of the CRU TS monthly high-resolution gridded multivariate climate dataset. *Sci. Data* **7**, 109 (2020).
74. Liang, S. et al. The Global Land Surface Satellite (GLASS) product suite. *Bull. Am. Meteorol. Soc.* **102**, E323–E337 (2021).
75. Hamed, K. H. & Ramachandra Rao, A. A modified Mann–Kendall trend test for autocorrelated data. *J. Hydrol.* **204**, 182–196 (1998).
76. Xu, J. et al. Data and Code for paper titled with "Global drought shows no detectable recent acceleration under climate warming". *Zenodo* https://doi.org/10.5281/zenodo.20455711 (2026).

Author contributions

Y.F. designed the study with input from all authors. J.X. and X.Z. collected data and performed analyses. Z.D. and Y.L. assisted with data processing and SPEI calculation. J.X. and Y.F. drafted and finalized the manuscript. X.Z., K.A.M., A.B., S.Z., and J.Y. reviewed and edited the manuscript. All authors contributed to the development of the manuscript.

Funding

Y.F., J.X., X.Z., Z.D., and Y.L. acknowledge support from Guangdong Basic and Applied Basic Research Foundation (2025A1515510023), Shenzhen Science and Technology Program (ZDSYS20220606100806014), and the Scientific Research Start-up Funds (QD2023021C) from Tsinghua Shenzhen International Graduate School. X.Z. acknowledges the support from the project of Hubei Key Laboratory of Basin Water Security, Wuhan, China (QTKS0034W25089). K.A.M. acknowledges funding from NSF grant AGS-2129576, an NSF CAREER award (AGS-2441565), and a Sloan Research Fellowship (FG-2023-19963). A.B. acknowledges the support of the Natural Sciences and Engineering Research Council of Canada (NSERC, Discovery Grant RGPIN/04501-2023). S.Z. acknowledges the support of the National Natural Science Foundation of China (grants 42471108 and 42521001).

Competing interests

The authors declare no competing interests.

Additional information

Supplementary information The online version contains supplementary material available at https://doi.org/10.1038/s43247-026-03954-6.

Correspondence and requests for materials should be addressed to Yuanchao Fan.

Peer review information *Communications Earth & Environment* thanks the anonymous, reviewer(s) for their contribution to the peer review of this work. Primary Handling Editors: Zhongjing Jiang and Nicola Colombo. A peer review file is available.